Monochromatic X-ray-induced thermal effect on four-reflection "nested" meV-monochromators: dynamical diffraction theory and finite-element analysis

HU Ling-Fei(胡凌飞) GAO Li-Dan(高立丹) LI Zhen-Jie(李贞杰) WANG Shan-Feng(王山峰)
SHENG Wei-Fan(盛伟繁) LIU Peng(刘鹏) XU Wei(徐伟)[1)]

BSRF, Institute of High Energy Physics, Chinese Academy of Sciences, Beijing 100049, China

Abstract: The high energy resolution monochromator (HRM) is widely used in inelastic scattering programs to detect phonons with energy resolution, down to the meV level. Although the large amount of heat from insertion devices can be reduced by a high heat-load monochromator, the unbalanced heat load on the inner pair of crystals in a nested HRM can affect its overall performance. Here, a theoretical analysis of the unbalanced heat load using dynamical diffraction theory and finite element analysis is presented. By utilizing the ray-tracing method, the performance of different HRM nesting configurations is simulated. It is suggested that the heat balance ratio, energy resolution, and overall spectral transmission efficiency are the figures of merit for evaluating the performance of nested HRMs. Although the present study is mainly focused on nested HRMs working at ^{57}Fe nuclear resonant energy at 14.4 keV, it is feasible to extend this to other nested HRMs working at different energies.

Key words: dynamical diffraction theory, high energy resolution monochromator, heat load

PACS: 41.50.+h, 42.25.-p, 61.05.cc **DOI:** 10.1088/1674-1137/39/9/096004

1 Introduction

The High energy-Resolution Monochromator (HRM) is one of the key optical elements in inelastic X-ray scattering (IXS) and nuclear resonant scattering (NRS) beamlines [1]. The monochromization can be achieved either by the backscattering geometry for IXS or by the multi-bounced crystal configuration for NRS and IXS [2]. Two aspects of merit are of crucial importance for the performance of the HRMs. One is the energy resolution, which is at the level of 10^{-7}–10^{-8} for most silicon based HRMs. The other is the integrated transmission or spectral efficiency. There is always a trade-off between the energy resolution and the integrated transmission depending on the purpose of the applications [1].

Many HRMs are based on a "nested geometry" using two channel-cut monolithic crystals [3–6]. As shown in Fig. 1, the nested HRM consists of two blocks of crystals which are nested together. The crystals are in (++−−) configuration [7]. More details about HRMs can be found in Toellner's review [1].

Heat load is another critical issue for many monochromators, especially for those used in third generation light sources. Due to thermally-induced deformations of the crystal [8], the performance of monochromators will deteriorate unless cryogenic or water cooling is introduced. To reduce the amount of heat and maintain good performance of the HRM, a high heat load monochromator (HHLM) is always mounted before the HRM in the IXS or NRS beamline. Nevertheless, the heat issue of HRM still requires special care, particularly for the high-index crystals which give rise to the high energy resolution. Toellner [9] reported a brilliant way to improve the performance of HRMs by cooling the high-index crystal down to 123 K in a specially designed cryostat. However, the heat issue for nested HRMs is not resolved due to the spatial limitations of the nested HRMs.

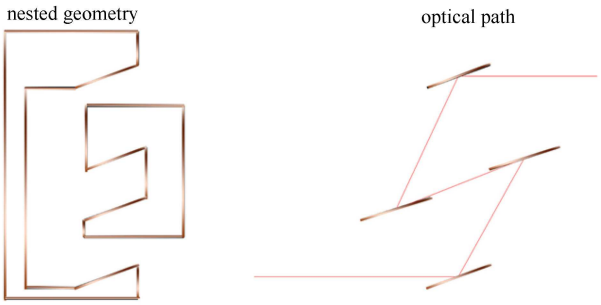

Fig. 1. Nested geometry of HRM and corresponding optical path.

Received 20 January 2015

1) E-mail: xuw@ihep.ac.cn

In this work, we provide a comprehensive theoretical analysis of the heat effects on (++−−) nested HRMs based on dynamical diffraction theory and finite element analysis. By comparing the performance of the HRMs, i.e. the energy resolution, integrated throughput, and power density ratio of the inner crystal pair, we propose a criterion for designing HRMs and a feasible approach to tackling the heat issue in nested HRMs. The rest of this paper is organized in four parts: firstly, we provide the theoretical basis for nested HRMs; secondly, we investigate the thermal effects on the crystals and the final performance; thirdly, we compare the performance of several HRMs in detail in order to provide a criterion for evaluating different designs; and lastly, we propose a scheme to solve the heat issue in nested HRMs.

2 Models and theoretical methods

2.1 HRMs in nested configurations

To illustrate thermal behavior, we studied concrete examples of silicon-made nested HRMs in the same configuration while using different crystal planes. In Table 1 we list the crystal lattice index, asymmetric cut angle and ratio, Debye-Waller factor at room temperature, Bragg angle, and incident and output angles.

Scheme 1 is adopted from Toellner's design [1]. The next three schemes are selected to match the acceptance of asymmetric cut (975) crystal, as well as to reduce the thermal power by the first crystals reducing the bandpass.

Table 1. Four schemes of nested HRMs and relevant parameters.

scheme	lattice index	$\Theta_B/(^\circ)$	$\theta_{in}/(^\circ)$	$\theta_{out}/(^\circ)$	$\alpha/(^\circ)$	b	D_{in}/μrad	D_{out}/μrad	Temp. factor 1
1	(440)	26.62	88.13	38.63	−24.75	−0.04	22.2	0.93	0.88
2	(975)	80.41	−61.41	80.59	71	−2.92	1.07	3.11	0.54
3	(975)	80.41	80.59	−61.41	−71	−0.34	3.11	1.07	0.54
4	(440)	26.62	38.63	88.13	24.75	−23.96	0.93	22.2	0.88
scheme	lattice index	$\Theta_B/(^\circ)$	$\theta_{in}/(^\circ)$	$\theta_{out}/(^\circ)$	$\alpha/(^\circ)$	b	D_{in}/μrad	D_{out}/μrad	Temp. factor 2
1	(440)	26.62	87.58	39.18	−24.2	−0.05	19.5	1.06	0.88
2	(975)	80.41	−61.41	80.59	71	−2.92	1.07	3.11	0.54
3	(975)	80.41	80.59	−61.41	−71	−0.34	3.11	1.07	0.54
4	(440)	26.62	39.18	87.58	24.2	−18.37	1.06	19.5	0.88
scheme	lattice index	$\Theta_B/(^\circ)$	$\theta_{in}/(^\circ)$	$\theta_{out}/(^\circ)$	$\alpha/(^\circ)$	b	D_{in}/μrad	D_{out}/μrad	Temp. factor 3
1	(511)	24.30	86.70	44.70	−21	−0.08	13.07	1.06	0.90
2	(975)	80.41	−61.41	80.59	71	−2.92	1.07	3.04	0.54
3	(975)	80.41	80.59	−61.41	−71	−0.34	3.11	1.07	0.54
4	(511)	26.62	44.70	86.70	21	−12.34	1.06	13.07	0.90
scheme	lattice index	$\Theta_B/(^\circ)$	$\theta_{in}/(^\circ)$	$\theta_{out}/(^\circ)$	$\alpha/(^\circ)$	b	D_{in}/μrad	D_{out}/μrad	Temp. factor 4
1	(444)	33.28	84.22	29.22	−27.5	−0.12	9.12	1.05	0.82
2	(975)	80.41	−61.41	80.59	71	−2.92	1.07	3.11	0.54
3	(975)	80.41	80.59	−61.41	−71	−0.34	3.11	1.07	0.54
4	(444)	33.28	29.22	84.22	27.5	−8.67	1.05	9.12	0.82

2.2 Methods

The dynamical diffraction theory is implemented using the Matlab® package. To analyse the thermal deformation and heat distribution, we employed finite element analysis (FEA) as implemented in commercial software ANSYS®. To further study the performance of the aforementioned HRMs, ray-tracing was conducted using the XOP-SHADOWVUI [10] package. In Table 2, we list the critical physical parameters of the silicon that was used in this work.

2.2.1 Implementation of dynamical diffraction theory

A. Bragg diffraction and twobeam approximation

In the case of Bragg-geometry diffraction with the two-beam approximation, the dynamical diffraction theory (DDT) can be formulated as [11]:

$$[k^2(1-\Gamma F_0)-(\boldsymbol{K}_0\cdot\boldsymbol{K}_0)D_0]-k^2P\Gamma F_{\bar{\mathrm{H}}}D_{\mathrm{H}}=0, \quad (1)$$

$$-k^2P\Gamma F_{\mathrm{H}}D_0+[k^2(1-\Gamma F_0)-(\boldsymbol{K}_{\mathrm{H}}\cdot\boldsymbol{K}_{\mathrm{H}})D_{\mathrm{H}}]=0, \quad (2)$$

with

$$\Gamma=r_e\lambda^2/\pi V, \quad (3)$$

Table 2. Basic information of Si.

working energy E/eV	14412.5
ambient temperature T	300K(26.85 ℃)
coefficient for thermal expansion β/K^{-1}	2.616×10^{-6}
lattice parameter a/nm	0.542109
Debye temperature Θ/K	530

$$F_{\rm H}=\sum_n (f^0(\boldsymbol{H})+f'(\lambda)+if''(\lambda))_{\rm n}\exp(2\pi{\rm i}\boldsymbol{H}\cdot\boldsymbol{r}_{\rm n})\exp(-M), \tag{4}$$

where k is the vacuum value of the wave vector; $r_{\rm e}$ is the classical electron radius, which equals 2.818×10^{-13} cm; V is the volume of the unit cell; P is the polarization; P=1 for σ polarization and P=cos2θ for π polarization; F_0, $F_{\rm H}$, $F_{\overline{\rm H}}$ are the structure factors of the crystal; f^0 is the atomic scattering factor; and, f' and f'' are the anomalous scattering corrections. The term $\exp(-M)$ represents the Debye-Waller factor and is temperature dependent. D_0 and $D_{\rm H}$ are the electric displacement vectors inside the crystal, corresponding to the refracted and diffracted directions, respectively.

The reflectivity of an infinitely thick crystal can be obtained by [12]:

$$R=\gamma\frac{|D_{\rm H}|^2}{\left|D_0^{(a)}\right|^2}=\left|\frac{\chi_{\rm H}}{\chi_{\overline{\rm H}}}\right|\left|\eta-S(\eta_{\rm r})\sqrt{\eta^2-1}\right|^2, \tag{5}$$

where

$$\chi_{\rm H} = -\Gamma F_{\rm H}, \chi_{\overline{\rm H}}=-\Gamma F_{\overline{\rm H}}, \tag{6}$$

$$\gamma = \frac{\gamma_0}{\gamma_{\rm H}}=\frac{\sin(\eta_{\rm H}+\theta_{\rm B})}{\sin(\eta_{\rm H}-\theta_{\rm B})}, \tag{7}$$

$$\eta = \frac{(\theta-\theta_{\rm B})\sin2\theta_{\rm B}+\chi_0(1-\gamma)/2}{|P|\sqrt{|\gamma|}\sqrt{\chi_{\rm H}\chi_{\overline{\rm H}}}}, \tag{8}$$

$\left|D_0^{(a)}\right|^2$ represents the incident intensity. γ is the asymmetry ratio, and η is the deviation parameter, which characterizes the deviation from the Bragg condition. $\eta_{\rm H}$ is the asymmetry angle. $S(\eta_{\rm r})$ is the sign (negative or positive) of real part of η. With the reflectivity calculated as above, we may deduce many important properties of single crystal reflection, such as the Darwin width, or the width between η=−1 and η=1.

B. Diffraction from multi-bounce crystals

The reflectivity function of a multi-crystal is given by:

$$R_{\rm total}(E,\theta)=\prod_i R_i(\theta_i), \tag{9}$$

where i denotes the ith crystal; R_i is the reflectivity of the ith crystal, which is described in the previous section; and, θ_i is the incident angle. We point out that the incident angle of the ith crystal equals the emergent angle of the $(i-1)$th crystal. The relation of the incident angle and the emergent angle of the ith crystal can be written as:

$$\sin\theta_i'=\sin\theta_i+\lambda/d_{\rm hkl}\cos(\eta_{\rm H}), \tag{10}$$

where θ_i denotes the emergent angle of the ith crystal and θ_i' denotes the incident angle. By integrating total reflectivity over the incident angle, the angle of the first crystal, we have:

$$T(E)=\int R_{\rm total}(E,\theta_1){\rm d}\theta_1. \tag{11}$$

The full width at half maximum (FWHM) of $T(E)$ is defined as the energy resolution of the monochromator. In addition, we define the maximum of $R_{\rm total}(E,\theta)$ as the peak reflectivity.

2.2.2 Finite element analysis of heat/temperature distribution

For nested HRMs, the temperature difference between the inner pair of high index crystals will significantly influence the performance. Therefore, in our FEA analysis we mainly focus on the inner pair of [975] crystals. The thermal boundary conditions are the same for these two crystals. In our present discussion, the thermal boundary condition for the crystal surface which is illuminated by the monochromatized light is set as a natural boundary condition (or the second boundary condition) while the other surfaces are set as mixed boundary conditions (or the third boundary conditions).

2.2.3 Ray-tracing of HRMs with same source

The ray-tracing is performed using XOP-SHADOWVUI. A Gaussian source was assumed for all tracing works. The distribution of the source in the phase space is 1 mm (H) by 0.5 mm (V) in size and $\sigma\sim$26 μrad (H) by $\sigma\sim$20 μrad (V) in angular divergence. The central energy was set as 14.4125 keV.

3 Results and discussion

To be specific, we used the real beamline parameters [13] for our estimation of the thermal effects. The light source is an undulator, with K=0.6265 corresponding to the first harmonic energy of 14.4125 keV. The high heat load diamond [111] double crystal monochromator gives rise to 1 eV bandpass. With the source parameters given in Table 3, the thermal power of $[440]_1$ and following $[975]_2$ of Scheme 1 HRM (Table 1) is estimated to be about 46.2 mW and 34.6 mW, respectively. Owing to the strong reduction of bandpass by the high-order crystal, the thermal power of the $[975]_3$ crystal drops drastically to 0.036 mW. As shown in Fig. 2, we estimate the power density for $[975]_2$ and $[975]_3$ by considering the Gaussian distribution of the source.

To analyze the temperature effects, we first need to point out the factors that can be affected by temperature. One is the Debye-Waller factor [14]:

$$\begin{aligned}{\rm DWF} &= \exp(-M_{\rm j})=\exp\left[-B_{\rm T}\left(\frac{\sin\theta_{\rm B}}{\lambda}\right)^2\right]\\ &= \exp\left[-B_{\rm T}\left(\frac{1}{2d_{\rm H}}\right)^2\right],\end{aligned} \tag{12}$$

Table 3. Undulator parameters.

length/m	period/cm	tuning range/keV	source size/μm	divergence/μrad
2.4	2.70	6.7–16.0 (1st harmonic) 6.7–60 (1st to 5th harmonic)	Σ_x:276 Σ_y: 11	$\Sigma_{x'}$:12.7 $\Sigma_{y'}$6.7

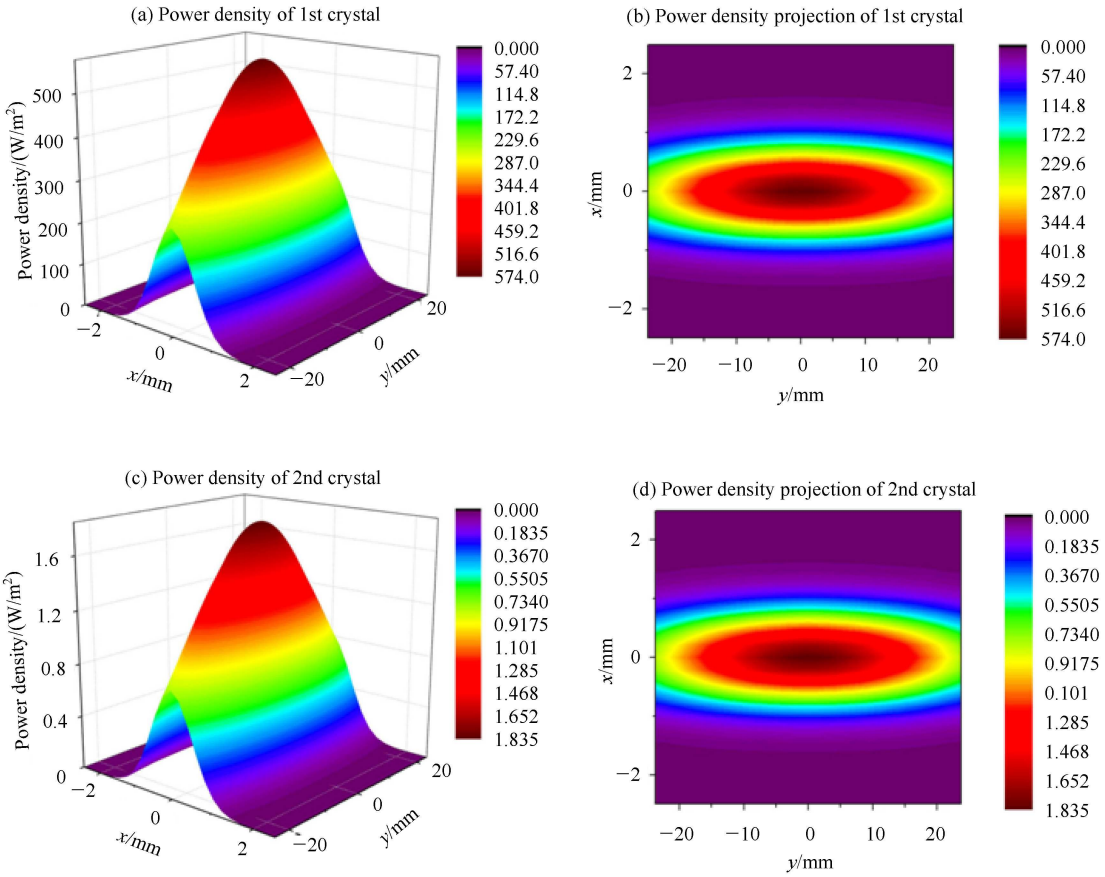

Fig. 2. (color online) (a) Power density on 1st [975] crystal; (b) Power density projected on the surface of 1st [975] crystal; (c) Power density of 2nd [975] crystal; and, (d) Power density projected on the surface of 2nd [975] crystal.

with

$$B_{\rm T}\left[\mathring{\rm A}^2\right]=\frac{11492T[{\rm K}]}{A\Theta^2[{\rm K}^2]}\phi\left(\frac{\Theta}{T}\right)+\frac{2873}{A\Theta[{\rm K}]}, \tag{13}$$

$$\phi(x) = \frac{1}{x}\int_0^x\frac{\xi}{{\rm e}^{\xi}-1}{\rm d}\xi, \tag{14}$$

$$d_{\rm H} = a/\sqrt{h^2+k^2+l^2}, \tag{15}$$

where DWF denotes Debye-Waller factor; $d_{\rm H}$ is the lattice spacing of diffraction plane $[hkl]$; a is the lattice parameter; h, k, and l are the Miller indices; A is the atomic mass number; and, Θ is the Debye temperature.

Another temperature-dependent factor is the lattice parameter a. The increasing temperature will cause thermal expansion of the silicon crystals. Given that the temperature variation is relatively small, the thermal expansion coefficient is a constant, and then the energy drift corresponding to the temperature variation is roughly given by [9]

$$\delta T_0=\frac{1}{\beta}\frac{\Delta E}{E}, \tag{16}$$

β is the coefficient of thermal expansion. For Si at 300 K [15], β=2.616×10^{-6} K^{-1}. From the formula given above, the energy drift is estimated to be 1 meV when the temperature changes by 26 mK.

3.1 FEA analysis of temperature distribution

With the estimated thermal power density (Fig. 2) as an input, the temperature distribution on the surface of the crystals can be estimated by FEA analysis while maintaining the ambient temperature at 26.85 ℃ (300 K). Fig. 3 gives the temperature distributions on the surface of the 1st and 2nd inner pair [975] of crystals. Clearly, the temperature gradient in the 1st crystal is

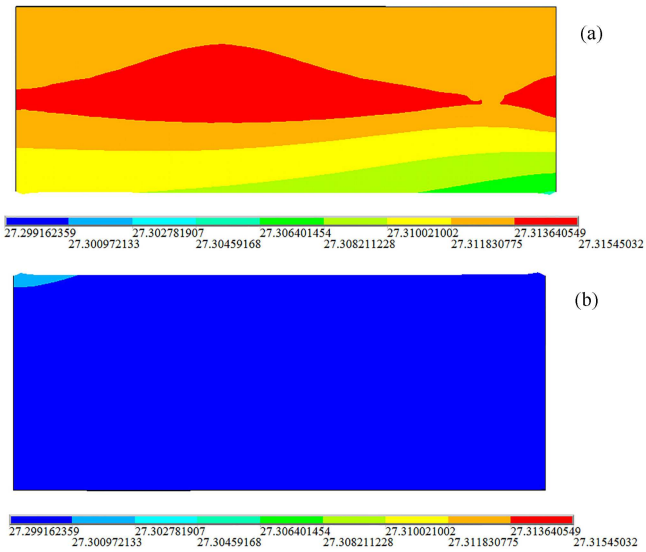

Fig. 3. (color online) (a) Temperature distribution of 1st [975] crystal (dimensions 56 mm×20 mm); (b) Temperature distribution of 2nd [975] crystal (dimensions 47.5 mm×20 mm).

significant while that for the 2nd crystal is negligible with a beam passing through the HRM. To be clearer, we draw a line through the central region of the crystals, where the temperature variation is larger than the rest. As shown in Fig. 4, the mean value of the 1st crystal temperature is 27.31459 ℃ and that of the 2nd crystal is 27.29967 ℃. The temperature difference between the $[975]_2$ and $[975]_3$ crystals is less than 20 mK.

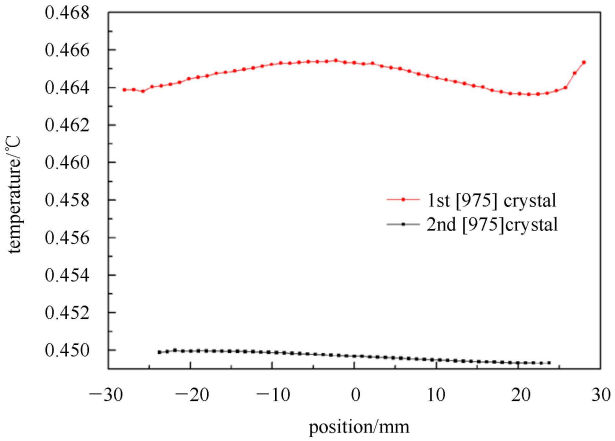

Fig. 4. (color online) Temperature difference between crystal surface and ambient temperature. The data is calculated crossing the central line of crystals.

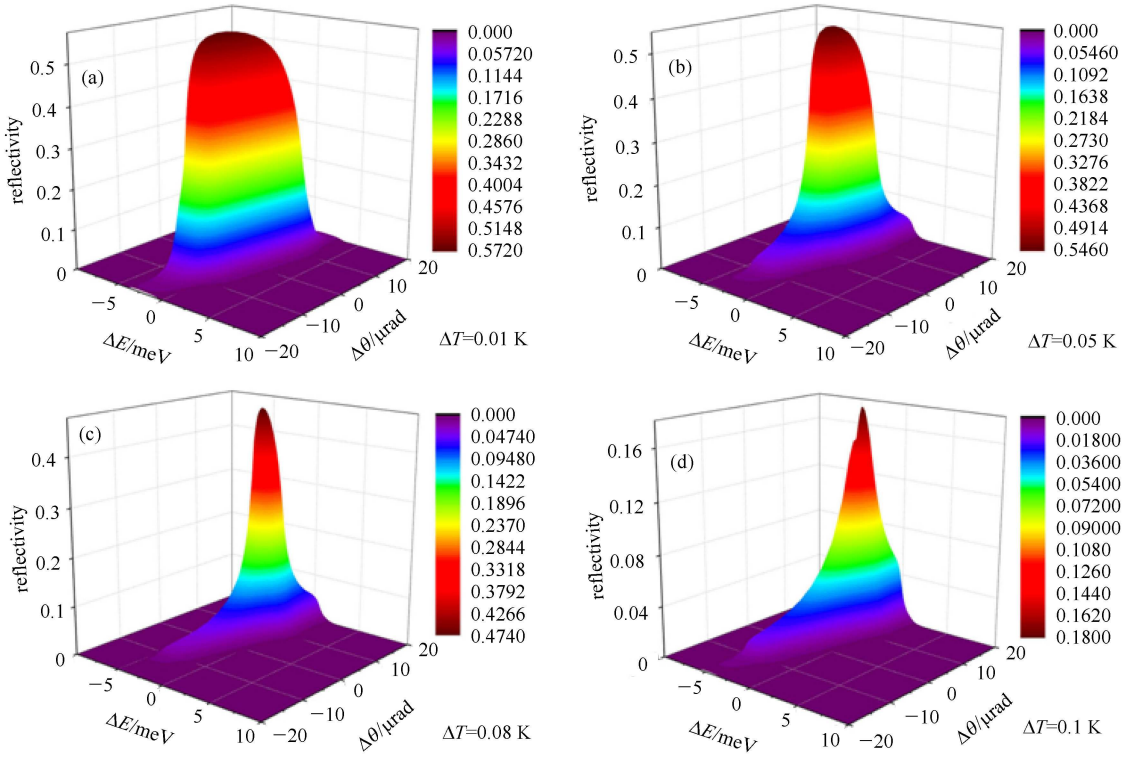

Fig. 5. (color online) 3D reflectivity diagram with temperature change of (a) 0.01 K; (b) 0.05 K; (c) 0.08 K; and, (d) 0.1 K.

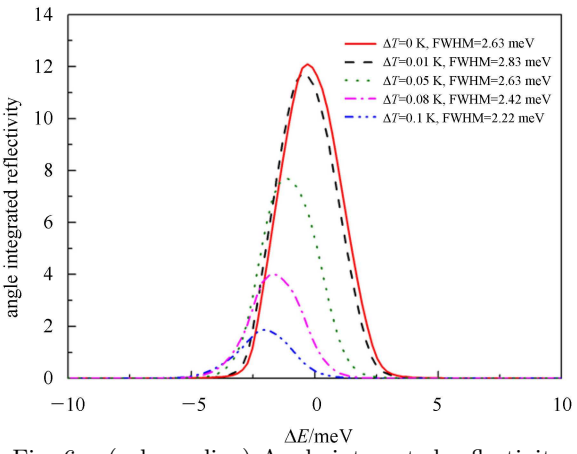

Fig. 6. (color online) Angle integrated reflectivity vs ΔE at different temperatures.

3.2 Performance of HRMs estimated from DDT

Temperature differences impose severe effects on the energy resolution and energy drifts of HRMs. In Fig. 5, we present the reflectivity of the HRMs as a function of energy as well as angle with different temperature differences. The obvious effects are the dropping of intensity and the drift of central energy. In Fig. 6, the angular-integrated reflectivity is compared for different temperatures. The energy resolution is affected slightly but the maximum reflectivity drops dramatically when the temperature increases by 100 mK. In Fig. 7 we compare the energy drift and peak reflectivity with respect to the temperature difference. With a 100 mK temperature difference, the energy drifts about 2 meV and then intensity drops by 20%.

3.3 Performance of HRMs estimated from ray-tracing

The performance of HRMs simulated by the ray-tracing approach is given in Fig. 8. The energy resolution of the four schemes remains at about 2.4–2.7 meV while

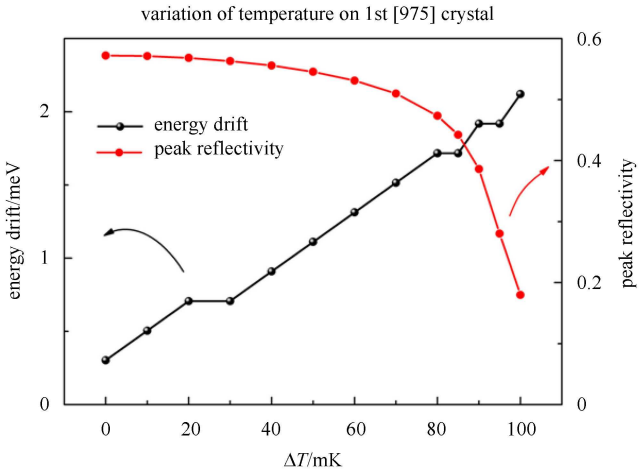

Fig. 7. (color online) Variation of temperature on 1st [975] crystal. Energy drift is defined as the difference between central energy and design energy.

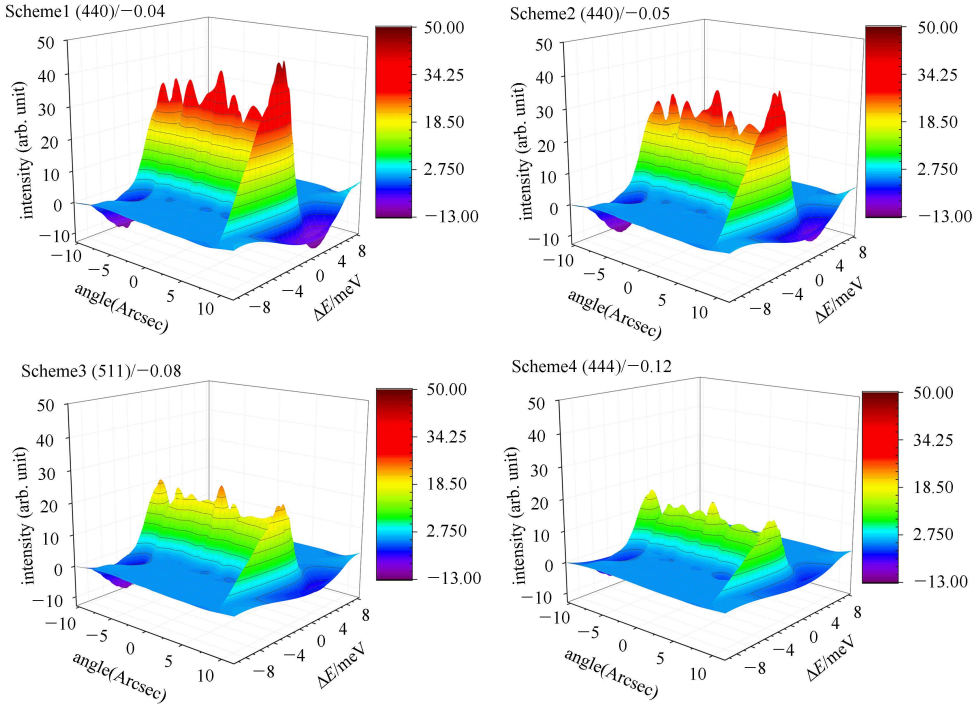

Fig. 8. (color online) The angle-energy distribution of intensity after different HRMs with the same light source. The parameters of the HRMs are given in Table 1.

the transmitted intensity changes greatly. For Scheme 1 and Scheme 2, the major difference is the asymmetric factor of the outer pair of crystals. The transmitted intensity of Scheme 2 is slightly lower than that of Scheme 1 while the energy resolution remains the same. Scheme 3 and Scheme 4 employ different crystal planes for the outer pair. Owing to the relatively narrower angular acceptance of [511] and [444] crystals, the transmitted intensity reduces by 30% and 57% for Scheme 3 and Scheme 4, respectively, with respect to that of Scheme 1. We also estimate the heat load on the inner pair crystals for all schemes. The temperature difference between the two crystal planes of the inner pair crystals are positively correlated with the heat load. We define the power ratio between the $[975]_2$ and $[975]_3$ as another criterion to evaluate the thermal effects of the nested HRMs. The corresponding power ratios are 966, 956, 1030, and 733 for Scheme 1, Scheme 2, Scheme 3, and Scheme 4, respectively. In comparison with the power ratio of Scheme 1, Scheme 2 and Scheme 4 have lower power ratios while Scheme 3 has a larger power ratio. By employing Scheme 4, the power ratio drops by 24% with respect to that of Scheme 1.

4 Conclusions

The high energy resolution monochromator (HRM) is a pivotal instrument in the inelastic scattering technique. Although a large portion of the heat load is dissipated by the pre-monochromator, using either cryogenically cooled Si[111] or water cooled diamond[111] double crystal, the temperature difference between the first and second crystal face of the inner pair of crystals in a nested HRM could cause energy drift and intensity reduction, thus deteriorating the performance of the HRM. By employing dynamical diffraction theory, finite element analysis, and ray-tracing, we have numerically studied the temperature effect, as well as its impact on the energy drift and transmitted intensity of HRMs. From the detailed analysis, it is concluded that the power ratio between the heated and less heated inner pair crystals is not linearly correlated with the transmitted intensity. Therefore, we propose power ratio as a third criterion along with energy resolution and transmitted intensity for designing nested HRMs. Our results could also be extended to the design of nested HRMs working at different energies. Furthermore, the heat load on the inner pair crystals, as demonstrated in our simulation, can be reduced using either the outer pair of crystals with a narrower band-pass or compensated by heating up the less heated crystal of the inner pair of crystals with a well-adjusted heater bearing using the same power distribution as caused by the X-ray.

We thank Dr. Thomas Toellner, Dr. E. E. Alp, Dr. Xianrong Huang, and Dr. Jiyong Zhao of the ANL APS for providing the prototype designs for the crystals and for their many fruitful discussions during the course of this study. We sincerely thank Prof. Xiaowei Zhang from KEK for his enlightening discussions. One of the authors (XU Wei) also thanks for Dr. Yong Cai of the BNL NSLSII for insightful discussions.

References

1 Toellner T. Hyperfine Interact, 2000, **125**: 3–28
2 Toellner T, HU M, Bortel G et al. Nucl. Instrum. Methods A, 2006, **557**: 670–675
3 Ishikawa T, Yoda Y, Izumi K et al. Rev. Sci. Instrum., 1992, **63**: 1015–1018
4 Leupold O, Pollmann J, Gerdau E et al. Europhys. Lett., 1996, **35:** 671
5 Toellner T, Mooney T, Shastri S et al. Proc. SPIE, 1992, **1740**: 218–221
6 Yabashi M, Tamasaku K, Kikuta S et al. Rev. Sci. Instrum., 2001, **72**: 4080–4083
7 Shvyd'ko Y. X-ray Optics: High-Energy-Resolution Applications. Springer, 2004. 143–165
8 ZHANG L, Sánchez del Río M, Monaco G et al. J. Synchrotron Radiat, 2013, **20**: 567–580
9 Toellner T, Alatas A, Said A et al. J. Synchrotron Radiat, 2006, **13**: 211–215
10 Sanchez del Rio M, Canestrari N, JIANG F et al. J. Synchrotron Radiat, 2011, **18**: 708–716
11 Batterman, Boris W. & Cole, H. Rev. Mod. Phys., 1964, **36**: 681
12 Authier A. Dynamical Theory of X-ray Diffraction. Springer, 2001. 85–87
13 YAN L, ZHAO J, Toellner T S et al. J. Synchrotron Radiat, 2012, **19**: 814–820
14 Als-Nielsen J & McMorrow D. Elements of Modern X-ray Physics. John Wiley & Sons, 2011. 172–176
15 Okada Y & Tokumaru Y. J. Appl. Phys.,1984, **56**: 314–320